Enzyme Dynamics and Tunneling Enhanced by Compression in the Hydrogen Abstraction Catalyzed by Soybean Lipoxygenase-1

Ismael Tejero,[†] Mireia Garcia-Viloca,*,[‡] Àngels González-Lafont,[†,‡] José M. Lluch,[†,‡] and Darrin M. York[§]

Departament de Química and Institut de Biotecnologia i de Biomedicina, Universitat Autònoma de Barcelona, 08193, Bellaterra (Barcelona), Spain, and Department of Chemistry, University of Minnesota, 207 Pleasant Street SE, Minneapolis, Minnesota 55455-0431

A fully microscopical simulation of the rate-limiting hydrogen abstraction catalyzed by soybean lipoxygenase-1 (SLO-1) has been carried out. This enzyme exhibits the largest, and weakly temperature dependent, experimental H/D kinetic isotope effect (KIE) reported for a biological system. The theoretical model used here includes the complete enzyme with a solvation shell of water molecules, the Fe(III)-OH$^-$ cofactor, and the linoleic acid substrate. We have used a hybrid QM(PM3/d-SRP)/MM method to describe the potential energy surface of the whole system, and the ensemble-averaged variational transition-state theory with multidimensional tunneling (EA-VTST/MT) to calculate the rate constant and the primary KIE. The computational results show that the compression of the wild-type active site enzyme results in the huge contribution of tunneling (99%) to the rate of the hydrogen abstraction. Importantly, the active site becomes more flexible in the Ile553Ala mutant reactant complex simulation (for which a markedly temperature dependent KIE has been experimentally determined), thus justifying the proposed key role of the gating promoting mode in the reaction catalyzed by SLO-1. Finally, the results indicate that the calculated KIE for the wild-type enzyme has an important dependence on the barrier width.

1. Introduction

Soybean lipoxygenase-1 (SLO-1), a nonheme iron dioxygenase, stereo- and regiospecifically catalyzes hydroperoxidation of 9(*Z*),12(*Z*)-octadecadieonic acid (linoleic acid, LA) to 13(*S*)-hydroperoxy-9(*Z*),11(*E*)-octadecadieonic acid (13(S)-HPODE). The reaction proceeds by an initial, rate-limiting abstraction of the pro-S hydrogen atom from the C_{11} position of linoleic acid by the Fe(III)-OH$^-$ cofactor, to generate linoleyl radical and reduced enzyme (Fe(II)-OH$_2$). O_2 rapidly adds to this radical and then abstracts a hydrogen atom from the water molecule, thus forming the hydroperoxide and regenerating the active, oxidized enzyme (Figure 1).

SLO-1 is commonly used as an analogue of the mammalian lipoxygenases, which have great physiological and pathological importance as they play key roles in the biosynthesis of leukotrienes and lipoxins.[1,2] Oxidative stress and carcinogenesis are associated with uncontrolled lipoxygenase activity, making these enzymes important pharmaceutical targets.[3–5]

SLO-1 has received increasingly extensive attention from both experimentalists and theoreticians for the past 15 years.[6–11] This is mainly due to the fact that the rate-limiting hydrogen abstraction exhibits the largest experimental H/D kinetic isotope effect (KIE) on k_{cat} ($k_H/k_D = 81$ at $T = 303$ K) so far reported for a biological system, along with a weak temperature dependence for both k_{cat} ($E_{a,H} = 2.1 \pm 0.2$ kcal/mol) and KIE ($E_{a,D} - E_{a,H} = 0.9 \pm 0.2$ kcal/mol) within the interval of temperatures 278–323 K.[12–16] This spectacular and extremely large KIE highly exceeds the kinetic isotope effects arising from isotope zero-point energy differences within a semiclassical model.[17] This fact together with the weak temperature dependence of the rate constants have been considered to be compelling experimental evidence for extensive quantum mechanical hydrogen tunneling in this enzymatic reaction. Therefore, SLO-1 has become the workhorse for studying hydrogen tunneling in enzymes. Tunneling can notoriously increase the catalytic rate of an enzyme.[18–20] This is a very challenging, but fundamental field aimed at the detailed understanding of the physical basis for the enormous catalytic power of these systems.

On the other hand, many bulky, aliphatic residues compress the substrate-binding pocket of SLO-1 (for instance, Leu546, Leu754, and Ile553). These residues provide a large surface to interact with the bound substrate. Mutating a large Ile or Leu side chain to an Ala side chain opens up space within the binding pocket of SLO-1, leading to an altered hydrogen transfer kinetics. So, for the mutants Leu754Ala and Leu546Ala the activation energy is larger than that for the wild-type SLO-1, the k_{cat} is up to 3 orders of magnitude smaller, and the KIE becomes slightly more temperature dependent. In contrast, the mutant Ile553Ala exhibits k_{cat} and activation energy values similar to the wild-type ones for the protiated substrate, although the KIE here is markedly temperature dependent.[15]

From the theoretical point of view, the huge complexity of the system renders it very difficult to do a detailed dynamical study of that hydrogen abstraction process including the whole enzyme, the solvent water molecules, and the real substrate. Different simplifications have been introduced instead. So, some papers have been recently devoted to the study of the structure

---

* Address correspondence to this author. E-mail:mireia@bioinf.uab.es.
[†] Departament de Química.
[‡] Institut de Biotecnologia i de Biomedicina.
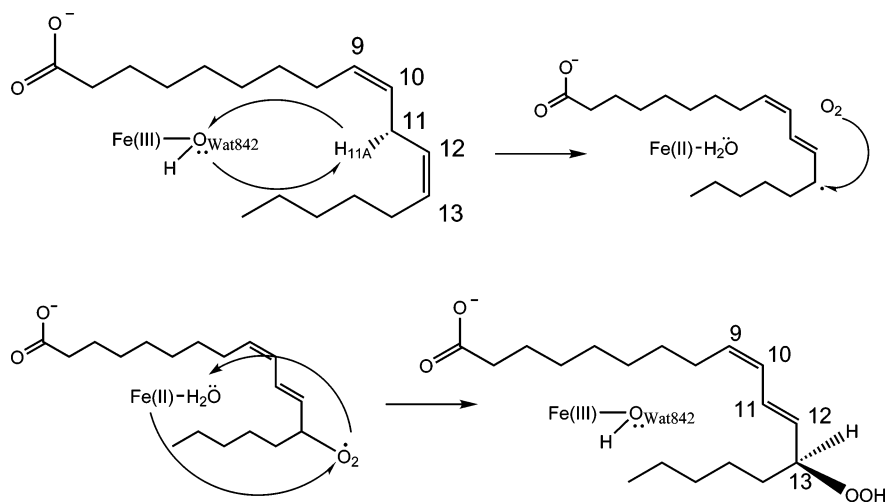[§] Department of Chemistry, University of Minnesota.

Figure 1. Schematic representation of the reaction catalyzed by SLO-1.

and catalytic reactivity of the active iron site of SLO-1, carrying out electronic structure calculations on just its first coordination sphere with the corresponding amino acids having been replaced by smaller models of them.[21−24] A second group of theoretical papers have studied very recently the dynamical aspects of the hydrogen abstraction in SLO-1, focusing on the calculation of rate constants and KIEs in different models of the real substrate−enzyme system. Klinman and co-workers[6] have used the fully nonadiabatic approach of Kuznetsov and Ulstrup.[25] No microscopical representation of the substrate−enzyme complex was made. The effective stretch between the hydrogen donor (C) and acceptor (O) atoms was used to account for the protein gating, which modulates the hydrogen abstraction barrier height and width, and, as a consequence, promotes the hydrogen tunneling. The effect of the environment was introduced by means of a parameter, the reorganization energy. Their results show that wild-type SLO-1 has a fairly stiff active site, probably optimized for hydrogen tunneling, gating being hindered, leading to a nearly temperature-independent KIE and a small activation energy. Interestingly, and in agreement with the above-mentioned site-directed mutagenesis experiments by the same authors,[15] when the hydrogen transfer distance is widened to some extension and the gating vibration mode is softened, the KIE becomes markedly temperature dependent.

Hillier and co-workers[26] have performed a microscopical, adiabatic treatment of the hydrogen abstraction by combining quantum mechanical (QM)/molecular mechanical (MM) electronic structure calculations with canonical variational transition state theory including multidimensional tunneling corrections. They have obtained an activation energy of 6.9 kcal/mol and a KIE at 300 K of 18.9 (the tunneling contribution was $\kappa_H/\kappa_D = 780/325 = 2.4$).

Siebrand and Smedarchina[27] have studied the temperature dependence of the KIE. They have used a model in which the tunneling coordinate, represented by two crossing Morse potentials (in a nonadiabatic treatment based on the Golden Rule formulation) or a single quartic double-minimum potential (in an adiabatic approximation), is assisted by a harmonic promoting mode. Their results contribute to explain a large KIE with weak temperature dependence.

Warshel and co-workers[28] have carried out a microscopical simulation where 1,4-pentadiene was taken as a short model of the linoleic acid, and all the protein atoms plus solvent molecules were included. The adiabatic treatment was based on the quantum classical path version of the centroid path integral

approach with an empirical valence bond (EVB) potential energy surface. The EVB surface was first parametrized by fitting to B3LYP calculations, and then it was refined to reproduce the experimental k_{cat} at 300 K. The calculations give a KIE of 86 at 300 K, although the method does not permit isolating the actual tunneling contribution to it.

Finally, Hammes-Schiffer and co-workers[29] have treated the hydrogen abstraction in SLO-1 as a nonadiabatic proton-coupled electron transfer reaction using a multistate continuum model. The solute was described by a multistate valence bond model in terms of four diabatic charge transfer electronic states involving the proton and the electron, and the transferring hydrogen nucleus is represented by a quantum mechanical wave function. No explicit microscopical representation of the protein was used. The inner-sphere reorganization energy due to the Fe−ligand bonds was estimated from B3LYP calculations, whereas the outer-sphere reorganization energy of the protein was calculated within the dielectric continuum approximation by using the frequency-resolved cavity model for conformations obtained with docking simulations on linoleic acid and SLO-1. Their results suggest that the large KIE is due to the relatively small overlap of the reactant and product proton vibrational wave functions and the dominance of the lowest energy reactant and product vibronic states in the hydrogen tunneling process.

After this short review of the field, it is clear that the distance that the hydrogen atom has to jump, the gating promoting mode, and its vibration frequency are some of the most relevant features of the rate-limiting hydrogen abstraction from linoleic acid by the Fe(III)-OH$^-$ cofactor in SLO-1, specially the unusual KIE. As a consequence, as shown by site-directed mutagenesis experiments,[15] the compression exerted by the bulky groups present in the substrate-binding pocket of SLO-1 is a key factor in the process. For this reason, a fully microscopical simulation of this hydrogen abstraction reaction including the complete enzyme with the corresponding solvation shell of water molecules, along with the real substrate (LA) and using a reliable electronic structure/dynamical theoretical method, is highly convenient to obtain a clear understanding of how this enzyme works. To this aim, we present in this paper a theoretical calculation that gathers all those factors at once. We have used here a QM/MM approach[30] along with ensemble-averaged variational transition-state theory with multidimensional tunneling (EA-VTST/MT)[31,32] to calculate the rate constant and the KIE of that intringuing rate-limiting hydrogen abstraction.

2. Computational Details

2.1. Model of the Enzyme−Substrate Complex in Water. This work uses, as an initial geometry, the SLO-1 PDB entry 1YGE in the Brookhaven Protein Data Bank, which is known to have 1.4 Å resolution.[33] This structure contains the Cartesian coordinates for the enzyme atoms. To the best of our knowledge, up to now no SLO-1 structure has been solved with a substrate. To dock the substrate in order to build a Michaelis complex structure, we used a SLO-1 isoform crystal structure (SLO-3, PDB entry 1IK3[34]), which has been solved with the final product 13(S)-HPODE in the active site. The active sites of both structures, SLO-1 and SLO-3, were overlapped with use of the ProFit software[35] with the aim to obtain a set of preliminary coordinates with the substrate within the SLO-1 active site. We transformed the product 13(S)-HPODE into the reactant LA by superimposing the common atoms between them. Then, to avoid bad contacts, a manual refinement of the substrate position was carried out.

The coordinates for hydrogen atoms of the protein and the substrate were determined by using the HBUILD facility in the program CHARMM.[36] The protonation states for all ionizable residues were set corresponding to pH 7. Histidine residues were modeled as neutral residues with the proton on N-epsilon (NE) or N-delta (ND) as determined on the basis of possible hydrogen bond interactions deduced from the original X-ray crystallographic structure.[33] The carboxylic end of LA was modeled unprotonated.

For comparison purposes, the mutant Ile553Ala was set up manually from the wild-type model at this point. The side chain of the Ile553 residue was substituted by a $-CH_3$ group. The common procedure used to solvate and to equilibrate the Michaelis complexes formed by the wild-type and the mutant enzymes with the substrate are described next.

We solvated both enzyme systems superimposing a sequence of water spheres of 30 Å radius on the proteins. Each sphere was centered at the center-of-mass position of the quantum mechanical region defined in the next section. Water molecules with the oxygen atom at a distance less than 2.5 Å from any heavy atom were removed, and this was repeated three times with randomly rotated water spheres. All the waters and the substrate/enzyme atoms within a 15 Å sphere around the center were minimized for 100 and 10 steps, respectively, with the adopted-basis set Newton−Raphson (ABNR) method in CHARMM-version c30a1. Then, a molecular dynamics (MD) simulation was carried out for the water molecules at 150 K for 5 ps. At this point, the whole solvation process was repeated to fill in additional cavities generated by the equilibration calculations. The final solvated wild-type system contains 17 837 atoms, including 51 substrate atoms and 4 509 water atoms. The mutant system contains a total of 17 816 atoms, of which 4 497 are water atoms.

2.2. Potential Energy Function. The QM/MM potential energy surface (PES) was calculated by using the interface between CHARMM[36] and MNDO97[37] programs. The system was partitioned into a quantum mechanical (QM) region consisting of 71 atoms and a molecular mechanical (MM) region containing the rest of the system. The QM region is depicted in Figure 2. It includes 17 atoms from the lipidic substrate, 11 atoms from each of the three histidine residues in the active site (His499, His504, and His690), 8 atoms from the Asn694, 3 atoms from the terminal Ile839, and the Fe(III)-OH⁻ cofactor able to accept the pro-S hydrogen (H_{11A}) atom from the linoleic acid. The boundary between the QM and the MM regions was represented by the link atom approach.[38] Seven link atoms were
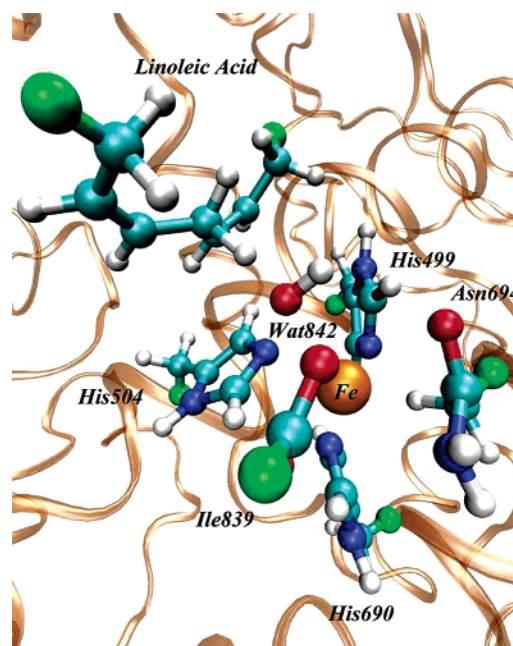

Figure 2. Active center in SLO-1. The QM atoms are represented in a ball-and-stick model (link atoms in green). See Figure 9 for a schematic representation of the active site.

used bonded to 5 Cα atoms of the 5 active site residues involved in the QM region, and 2 aliphatic C atoms which divide the lipidic substrate into two classical and one quantum parts. The MM region was represented by the CHARMM27[39] all-atom force field to represent the MM atoms of the protein and the three-point-charge TIP3P[40] model was used for water. Force field parameters for linoleic acid that are not strictly available in the CHARMM27 force field were derived from standard parameters for analogous lipid compounds.[41]

The QM subsystem was described by our own semiempirical PM3/d model, with specific reaction parameters (SRP)[42] for iron.[43] As described in ref 44, the goal of the reparametrization was to reproduce the B3LYP/6-311++G(3df,2p)/MM results for the hydrogen abstraction reaction in SLO-1. In the parameter optimization procedure, we used a database that included gas-phase cluster models[24] but also a final refinement to take into account the effect of the whole enzyme.

2.3. Simulations. Stochastic boundary molecular dynamics (SBMD) was used to treat the system,[44,45] which is divided into three regions: the reaction region, the buffer region, and the reservoir region. The reaction region contains the active center and all the waters and amino acid residues that have any atoms within 26 Å from the center-of-mass of the QM part, which is defined as the center of the system. In the case of the wild-type enzyme simulation that is 460 solute residues and 820 water molecules. The buffer region contains waters and amino acids that have any atoms within 30 Å from the center not belonging to the reaction region. This results in 169 solute residues and 654 water moecules. All other atoms (3 839 of a total of 17 837) were assigned to the reservoir region and were kept frozen in the MD simulations. The reaction region was treated by using Newtonian molecular dynamics. The buffer region represents a heat bath surrounding the reaction region and its dynamics was propagated by Langevin dynamics. The harmonic force constants and the friction constants used in the Langevin equations of motion were taken from previous works.[46] A deformable boundary potential[45] was imposed on water molecules at the buffer/reservoir interface to prevent them from

diffusing away and to represent the effect of bulk solvent outside this boundary. In all simulations, the three internuclear distances of the water molecules, with the exception of the quantum water (Wat842) in the active site, and all the bonds involving hydrogen atoms were frozen by the SHAKE algorithm.[47] We used the leapfrog integration scheme to propagate the equations of motion with an integration time step of 1 fs. A spherical cutoff distance of 13.0 Å, based on the center-of-mass separation between interacting groups, was used for the nonbonded interactions. To smoothly reduce the interaction energy to zero a switch function in the region from 12.0 to 13.0 Å was used. The nonbonded pair list was updated every 25 steps.

2.3.1. Michaelis Complex Preparation. Initially, the substrate molecule was relaxed in the active site by running 100 steps of QM/MM minimization by using the ABNR method and with the protein and water atoms kept fixed. From the resulting configuration, we performed 30 ps of SBMD simulations without additional restraints under the QM/MM potential, raising gradually the simulation temperature from 0 K to the experimental value of 303 K. Then, a further 120 ps of simulation at 303 K were carried out to equilibrate the system. At this point, we considered that our model of the Michaelis complex had reached an equilibrium state because of the small value of the fluctuations of the temperature (<2 K) and the total energy (0.25% of the average value) over the last 20 ps. The same procedure was used to obtain a model of the complex between the substrate and the Ile553Ala mutant. In this case, a total of 110 ps of SBMD were carried out. During the last 10 ps of the wild-type and mutant enzyme simulations, configurations were saved every 100 steps for later structural analysis.

2.3.2. Reaction Coordinate Definition and Potential Energy Profile of the Reaction. The reaction coordinate z is defined as the difference between the $C_{11}-H_{11A}$ distance (r_{break}) and the $H_{11A}-O_{Wat842}$ distance (r_{form}) (see Figure 1). To the aim of having a preliminary idea about the QM/MM potential energy surface (PES) in the condensed phase, we calculated the monodimensional potential energy profile for the hydrogen atom abstraction in the wild-type active site by a series of geometry optimizations of the mobile part of the system (see below) in the presence of harmonic restraints applied on the reaction coordinate z. First, the equilibrated Michaelis complex was minimized with the ABNR method until the norm of the gradient was less than 5×10^{-4} kcal/(mol Å). Then, the RESD module in CHARMM was used to define harmonic restraint terms of the form

$$V_{RESD} = \frac{1}{2}k_{RESD}(z - z^0)^2 \qquad (1)$$

where k_{RESD} is the restraining force constant, which was set equal to 2500.0 kcal/(mol Å²). The quantity z^0 is the reference value of the reaction coordinate z at each energy minimization calculation, which was increased with a step size of 0.025 Å. For each of the points defined by z^0, a minimization was carried out with a gradient tolerance of 0.001 kcal/(mol Å) and with the ABNR algorithm. In these restrained minimizations the reaction coordinate was projected out of the gradient and atoms outside a 30 Å sphere centered in the QM part were kept frozen.

From the product side structure, at the end of the first monodimensional PES scan, we carried out a second series of restrained minimizations with z^0 values that lead from products to reactants, then back to products, and go on until energy convergence was achieved in both senses.

2.3.3. Dynamics. We have used the Ensemble-Averaged Variational Transition State Theory with Multidimensional Tunneling (EA-VTST/MT)[31,32] to study the dynamics of the hydrogen abstraction catalyzed by the wild-type enzyme SLO-1. The theory and procedure used in this method is explained in previous papers[31,32,48,49] and therefore, here, we only give the computational details of this specific application study. The potential of mean force (PMF) $W^{CM}(T, z)$, along the reaction coordinate z as defined before, was determined by using the umbrella sampling technique.[50,51] Starting from the equilibrated Michaelis complex at 303 K, we performed a total of 17 separate simulations (windows) to span the entire range of the reaction coordinate from reactants to products. Each simulation i was carried out with a harmonic restraining potential (eq 1) centered at the location (z_i^0) of that particular window. The closer to the transition state region, the bigger the harmonic restraining force constant employed and the shorter the distance between the consecutive z_i^0 values. Different values of the restraining force constant were used in the range 40 to 190 kcal/(mol Å²). For each window, the starting structure and velocities were taken from the last structure of the previous window and the system was equilibrated for 20 ps. The probability density of configurations was collected and sorted into bins of width 0.01 Å for a subsequent 30 ps simulation. During the umbrella sampling simulations, the trajectory was saved every 10 steps. Overall, the PMF calculation has a total length of 850 ps. It is worth noting that, in this particular case, the wave function of the quantum part of the system, calculated at the PM3/d-SRP level, has a very slow convergence. This has prevented us of carrying out longer simulations. The classical free energy curve is finally obtained by using the weighted histogram analysis method (WHAM).[50,51]

To include quantum corrections to the classical free energy curve, we used CHARMMRATE,[52] based on an interface of the programs CHARMM,[36] MNDO97,[37] and POLYRATE.[53] We investigated two different systems and determined the primary kinetic isotope effects (KIEs): (i) the LA substrate with a protium atom at the H_{11A} position and (ii) the replacement of protium by a deuterium atom at this position. We defined a primary zone of 48 atoms over the total 71 quantum atoms. The quantum mechanical vibrational energy correction, $\Delta W_{vib}(T,z)$, to the computed PMF was obtained from instantaneous generalized normal-mode frequencies[54,55] of the primary zone atoms for 700 configurations generated along the $W^{CM}(T,z)$ curve (400 configurations of the product and the reactant windows and 300 configurations from two windows at the transition state zone of the $W^{CM}(T,z)$). The same configurations were used for both protium and deuterium quantized-vibrational corrections. For each configuration, the Hessian was determined numerically by a central difference scheme with a step size of 0.0053 Å, and the generalized normal modes were calculated in rectilinear mass-scaled coordinates.[56] When calculating generalized normal-mode frequencies, the reaction coordinate was projected out of the Hessian, as described in refs 54 and 55. The calculated frequencies for the various configurations were averaged over all the configurations that belong to a given bin of width 0.01 Å, and the quantum correction to the vibrational free energy, ΔW_{vib}, was calculated as a function of the averaged frequencies of 137 normal modes. The discrete values in individual bins were fitted to a fifth degree polynomial function to give the quantized-vibrational correction as a function of the reaction coordinate. The addition of this correction to the $W^{CM}(T,z)$ curve resulted in the quasiclassical PMF, $W^{(1)}(T,z)$, as described in ref 32. The generalized free energy of activation is calculated

TABLE 1: Selected Average Distances between Fe and Their Ligands r_{Fe-L} (Å), Linoleic Acid and the Second Coordination Sphere Residues r_{LA-SCS} (Å), and Hydrogen Bonds between Donor (D) and Acceptor (A) Atoms of Relevant Enzymatic Residues r_{D-A} (Å)[a]

				r_{Fe-L}			
	Fe	L	X-ray$_{SLO-1}$	X-ray$_{SLO-3}$	mutant (reactant)	reactant	TS	product
Fe−His499$_{518}$	Fe	NE2	2.23	2.23	2.441$_{(0.0016)}$	2.429$_{(0.0018)}$	2.429$_{(0.0024)}$	2.429$_{(0.0013)}$
Fe−His504$_{523}$	Fe	NE2	2.26	2.24	2.423$_{(0.0009)}$	2.434$_{(0.0009)}$	2.449$_{(0.0032)}$	2.478$_{(0.0009)}$
Fe−His690$_{709}$	Fe	NE2	2.21	2.28	2.396$_{(0.0021)}$	2.397$_{(0.0023)}$	2.448$_{(0.0024)}$	2.433$_{(0.0014)}$
Fe−Asn694$_{713}$	Fe	OD1	3.05	2.28	2.541$_{(0.0010)}$	2.516$_{(0.0012)}$	2.511$_{(0.0030)}$	2.516$_{(0.0020)}$
Fe−Ile839$_{857}$	Fe	OXT	2.40	2.05	2.360$_{(0.0014)}$	2.361$_{(0.0015)}$	2.376$_{(0.0016)}$	2.377$_{(0.0010)}$
	Fe	O	3.55	3.07	2.407$_{(0.0012)}$	2.414$_{(0.0012)}$	2.401$_{(0.0029)}$	2.409$_{(0.0031)}$
Fe−Wat842	Fe	OH2	2.56		2.435$_{(0.0008)}$	2.436$_{(0.0010)}$	2.449$_{(0.0036)}$	2.454$_{(0.0010)}$

				r_{LA-SCS}			
	LA	SCS	X-ray$_{SLO-1}$	X-ray$_{SLO-3}$	mutant (reactant)	reactant	TS	product
LA−Trp500$_{519}$	C10	CE3		4.11	4.181$_{(0.0085)}$	3.937$_{(0.0103)}$	4.084$_{(0.0163)}$	3.926$_{(0.0031)}$
	C12	CZ3		4.46	5.330$_{(0.0121)}$	4.574$_{(0.0119)}$	4.666$_{(0.0067)}$	5.105$_{(0.0139)}$
LA−Gln495$_{514}$	O1	NE2		8.98	3.564$_{(0.0106)}$	5.104$_{(0.0026)}$	4.305$_{(0.0035)}$	3.333$_{(0.0036)}$
	O2	NE2		9.11	3.949$_{(0.0097)}$	5.485$_{(0.0145)}$	4.414$_{(0.0241)}$	3.727$_{(0.0055)}$

				r_{D-A}			
	D	A	X-ray$_{SLO-1}$	X-ray$_{SLO-3}$	mutant (reactant)	reactant	TS	product
Gln697$_{716}$−Asn694$_{713}$	NE2	O	3.17	2.99	3.124$_{(0.0093)}$	2.887$_{(0.0049)}$	3.037$_{(0.0110)}$	2.865$_{(0.0021)}$
	NE2	OD1	3.12	3.38	3.081$_{(0.0088)}$	3.309$_{(0.0108)}$	3.880$_{(0.0100)}$	3.580$_{(0.0180)}$
Gln495$_{514}$−Gln697$_{716}$	NE2	OE1	3.03	9.19	2.994$_{(0.0052)}$	5.891$_{(0.0115)}$	5.213$_{(0.0310)}$	5.556$_{(0.0174)}$
His499$_{518}$−Gln495$_{514}$	ND1	OE1	3.59	6.22	3.308$_{(0.0050)}$	6.545$_{(0.0132)}$	5.806$_{(0.0350)}$	6.063$_{(0.0025)}$

[a] The numeration of residues corresponding to the SLO-3 enzyme is shown in smaller subscript type. The standard deviation of the values in our simulation is given in parentheses.

at this point and is called $\Delta G_{act}^{(1)}$. It yields the quasiclassical rate constant based on the single reaction coordinate z given by:

$$k^{(1)}(T) = \frac{k_B T}{h} \exp\left(-\frac{\Delta G_{act}^{(1)}}{k_B T}\right) \qquad (2)$$

where k_B is Boltzmann's constant, h is Planck's constant, and T is the temperature.

To calculate the averaged transmission coefficient by the static-secondary-zone (SSZ) approximation, we had 15 configurations from the classical simulation which define the transition state ensemble (TSE). These configurations were chosen on the basis of their closeness to z_*^{QC} (all of them belong to the interval $z_*^{QC} \pm 0.02$ Å), which is the value of the reaction coordinate at the maximum of the quasiclassical potential of mean force ($W^{(1)}(T,z_*^{QC})$). Visual inspection of the active center in this set of 15 configurations suggested that they can be classified in three categories depending on how much the lipid tails close over the active site. The sum of the values of the dihedral angles $C_8-C_9-C_{11}-O_{Wat842}$ and $C_{13}-C_{14}-C_{11}-O_{Wat842}$ (see Figure 1) provides a quantitative estimation of the compression. The results of this analysis indicated that the ratio between these categories, big/medium/small active site compression, was 1:3:1, respectively, with average values of the sum of the dihedral angles of 135°/164°/181°, respectively. As a consequence, we finally chose five members of the TSE following this ratio.

Geometry optimizations of the primary zone reactant and product species were performed by using the BFGS method, while the saddle point geometry was obtained by using the Newton−Raphson method with Brent line minimization[57] with the gradient converged to 5×10^{-8} atomic units. The minimum energy paths were traced by using the Euler steepest descent method[58] in mass-scaled coordinates with a reduced mass of 1 amu and a step size of 0.005 bohr. For each configuration of the TSE we calculated an individual quasiclassical recrossing

factor, $\Gamma_i(T)$, as described elsewhere,[31,48] and an individual semiclassical transmission coefficient accounting for multi-dimensional tunneling, $\kappa_i(T)$. The introduction of the quasi-classical recrossing correction, given by the average value of Γ_i, $\Gamma(T) = \langle\Gamma_i\rangle$, into the transition state rate constant $k^{(1)}(T)$ gives the final quasiclassical rate constant:

$$k^{QC}(T) = \Gamma(T)k^{(1)}(T) \qquad (3)$$

The five individual semiclassical transmission coefficients $\kappa_i(T)$ were not microcanocally optimized between the small-curvature tunneling (SCT) and the large-curvature tunneling (LCT) values as has been done in previous works.[48,49] As noted above, the wave function optimization is very time-consuming in this system and we could not afford the more time-demanding LCT calculations. Thus, the individual $\kappa_i(T)$ were calculated by the centrifugal-dominant small-curvature semiclassical adiabatic algorithm.[59] The product of the two factors, Γ_i and κ_i, gives the net transmission coefficient for configuration i, γ_i, which averaged over the five TSE members gives the final ensemble-averaged transmission coefficient, $\gamma(T)$. The final expression of the EA-VTST/MT rate constant is given by

$$k^{EA-VTST/MT}(T) = \gamma(T)k^{(1)}(T) \qquad (4)$$

The final theoretical estimate of the phenomenological free energy of activation is

$$\Delta G_{act}^{EA-VTST/MT} = \Delta G_{act}^{(1)} - RT \ln \gamma \qquad (5)$$

3. Results and Discussion

3.1. Michaelis Complexes for the Wild-Type SLO-1 Enzyme and the Mutant Enzyme. The first seven rows in Table 1 show the calculated average distances between iron and its ligands (see Figure 2) in the active sites of the modeled Michaelis complexes (sixth column and seventh column for the mutant and the wild-type enzymes, respectively) in comparison
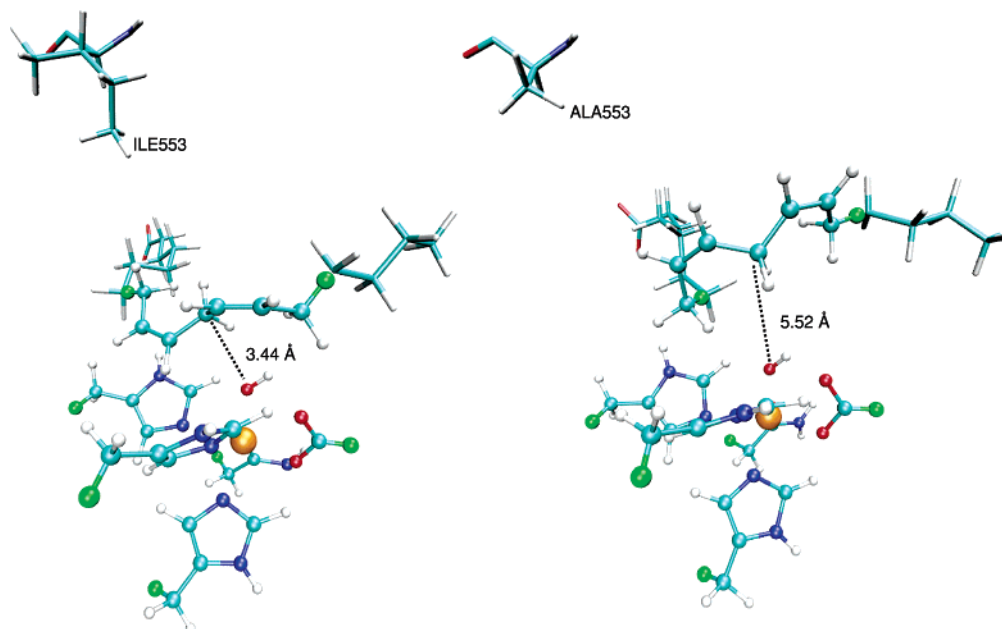
Figure 3. Distance between C_{11} and O_{Wat842} (joined by dotted lines) and relative position of the residue 553 with respect to the active center in both wild-type and mutant Ile553Ala Michaelis complexes.

to the values obtained by X-ray crystallography for SLO-1 without substrate (fourth column) and SLO-3 including the final product (fifth column). As observed in Table 1 in ref 35 the Fe coordination sphere in the SLO-1 and SLO-3 enzymes without substrate is comparable, which justifies the use of the data obtained for the SLO-3−product complex as a reference to validate our model of the SLO-1−substrate complex. The average interaction distances between Fe and the histidine ligands is within 0.2 Å of the experimental values. In contrast, the calculated Fe−Asn694 distance is 0.54 Å shorter than in the wild-type SLO-1 crystal structure and 0.23 Å longer than the distance found in the crystallographic structure of the isoform enzyme SLO-3 with the final product bounded. Experimental results provide evidence for the weakness of this Fe−Asn694 bond.[60] The two crystal structures reported in Table 1 show the decrease of three distances in going from the X-ray$_{SLO-1}$ to the X-ray$_{SLO-3}$, that is, the Fe−Asn694, the Fe−Ile839, and the Fe−Wat842 interactions. Our results for the model of the wild-type Michaelis complex where the metal is in its ferric form present an Fe−Asn694 distance of 2.51 Å, which confirms the weakness of this bond. In addition, the two oxygens of the terminal Ile839 are bounded to the metal with longer interaction distances than the monodentate interaction between this residue and Fe in the crystal structures. On the other hand, the comparison between columns six and seven indicates that the mutation of Ile553, which belongs to the second coordination sphere of the metal (see Figure 3), by an Ala residue does not significantly change the first coordination sphere of the metal.

Figure 4 is a partial view of a snapshot of the equilibrated complex between the wild-type enzyme and the substrate, where the interactions r_{LA-SCS} and r_{D-A} shown in Table 1 are marked with a dotted line. The following four rows in the table show the interaction distances between the LA substrate and two enzymatic residues. The Trp500 residue is found to have a $\pi-\pi$ stacking interaction with the product molecule double bonds in the SLO-3 crystal structure.[61] The distances shown in Table 1 between the LA substrate and the Trp500 residue indicate that this interaction is also found in our model of the equilibrated Michaelis complex, both for the wild-type and the mutant enzyme. Besides the interaction with Trp500, we have only

found one more interaction between the LA substrate and the enzyme (this one not referenced anywhere), that is, the hydrogen bonds between the −NH$_2$ group of the Gln495 residue and the carboxylate end of the substrate. The data in Table 1 indicate that in our simulation this interaction is formed during the hydrogen atom abstraction (as will be discussed later). The carboxylate end of the substrate in the Michaelis complex is not interacting with any enzymatic residue, but with water molecules. The Arg707 residue, which is proposed to form charge−charge interactions with the carboxylate end of the LA susbtrate,[61] is too far from our LA substrate in the equilibrated reactant or product complex wild-type enzyme.

Finally, the last four rows of Table 1 list the distances between enzymatic residues that are proposed to participate in an extensive hydrogen bonding network that connects the weakly bound asparagine ligand (Asn694) via the two second coordination sphere residues, Gln697 and Gln495, to an equatorial iron ligand, His499[62] (see Figure 4). The hydrogen bond distances found between these residues in the SLO-1 crystal structure are reported in Table 1. On the basis of these results, together with computational results on a gas-phase model,[63] and recent kinetic, crystallographic, and spectroscopic studies on mutant enzymes where the hydrogen bonding network is broken,[62] it has been suggested that the protein can control the Fe−Asn694 distance and, in turn, the enzyme activity via the hydrogen bond between Asn694 and Gln697, which changes the orientation of the metal ligand (Asn694).[62] The X-ray structure of the SLO-3−product complex indicates that the interactions of Gln495 with Gln697 and His499 are lost when the product is bounded in the active site. Importantly, these hydrogen bonds are also broken in the calculated Michaelis complex of the wild-type enzyme, while the interactions between Asn694 and Gln697 are conserved, in agreement with the experimental results.[34] These results support the proposal that when the substrate enters into the active site the hydrogen bond between Gln697 and Gln495 breakes and the Asn694 orientation changes.[62] On the contrary, the theoretical results for the mutant enzyme suggest a more relaxed active site that mantains the hydrogen bonding network despite the presence of the substrate. Importantly, the kinetic behavior of this mutant has also been related to this structural difference
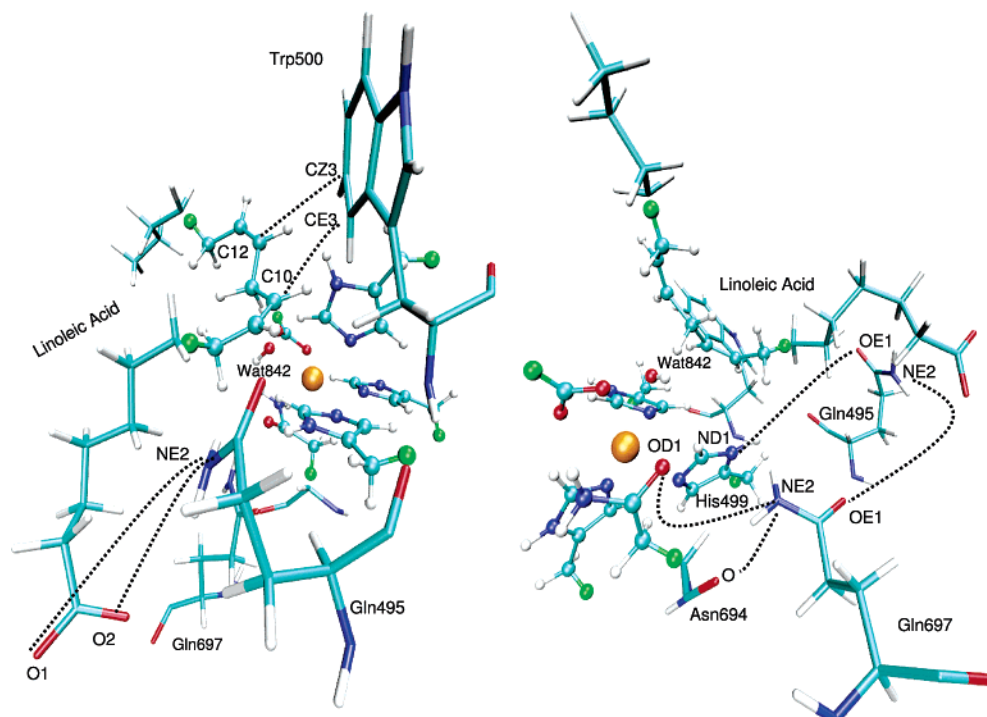
Figure 4. Partial views from a snapshot of the equilibrated complex between the wild-type enzyme and the substrate. The r_{LA-SCS} interactions are shown on the left side, whereas the r_{D-A} interactions are shown on the right side. All these interactions are marked with a dotted line and summarized in Table 1.

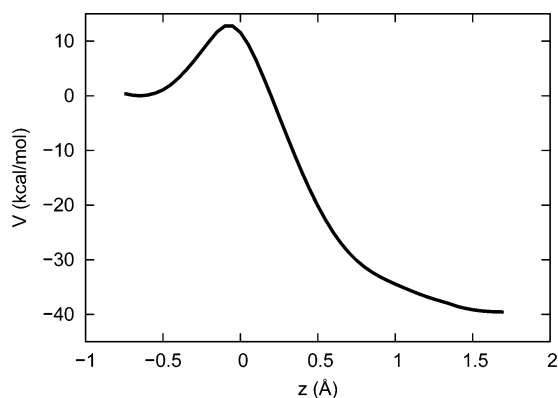**Figure 5.** Computed potential energy profile for the hydrogen abstraction in the active site of soybean lipoxygenase 1.

Figure 6. Computed potential of mean force for the hydrogen abstraction in the active site of soybean lipoxygenase 1: classical mechanical potential (red); including the vibrational correction for protium (green). The curve including the vibrational correction for deuterium is not depicted because it would appear superimposed to the protium curve at the scale used in this figure.

between the wild-type and the mutant enzyme active sites,[64] as will be commented on later.

3.2. QM/MM Potential Energy Profile and Classical Free Energy Curve for the Hydrogen Atom Abstraction. The converged potential energy profile for the hydrogen atom abstraction is shown in Figure 5. The potential energy barrier is determined to be 12.9 kcal/mol, with its maximum at $z = -0.1$ Å. The reactant and product are located at values of z of -0.65 and 1.7 Å, respectively, and the reaction is exoergic by 40 kcal/mol. At the maximum potential energy point the donor−H distance is 1.3 Å and the acceptor−H distance is 1.4 Å. These results can be compared to the results obtained in previous studies for different gas-phase models of the SLO-1 active site.[24] In general, the comparison suggests that the enzyme environment has two important effects with respect to the situation in the gas phase: to compress the active site, decreasing the distance in terms of the geometric reaction coordinate z between reactants and products by 3.80 Å, and to make the reaction more exoergic. Although the numerical value of the exoergicity is probably somehow exaggerated by the QM/MM
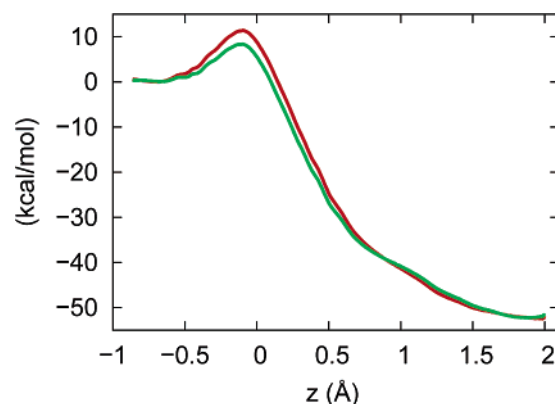
potential, this last effect has also been found in previous models of this enzymatic system[26,28] and suggests that the compression of the active site destabilizes the reactant with respect to the product.

On the other hand, the similarity between the QM/MM potential energy profile in Figure 5 and the classical mechanical potential of mean force (CM PMF or classical free energy curve) in Figure 6 indicates that the thermal and entropic contributions to the free energy are small. Thus, Figure 6 shows that the transition state of the CM PMF is located at $z_*^{CM} = -0.095$ Å. The values of z at the reactant ($z_R = -0.68$ Å), transition state (z_*^{CM}), and product ($z_P = 1.9$ Å) are close to the values obtained for the corresponding minimized structures of the potential energy curve. Figure 7 shows the evolution of the distance between the donor and the accceptor atoms along the reaction as a function of z, where this distance has been averaged
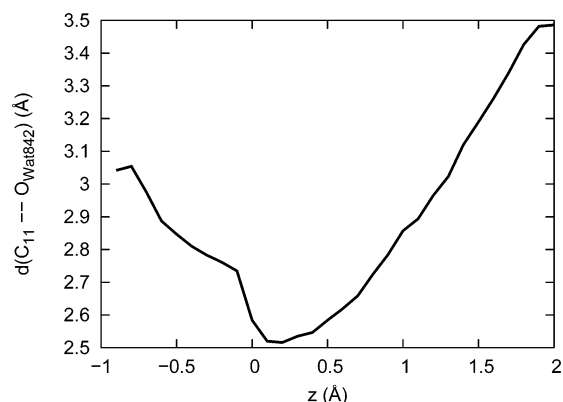
Figure 7. Average distance between the donor and the acceptor atoms as a function of the reaction coordinate.
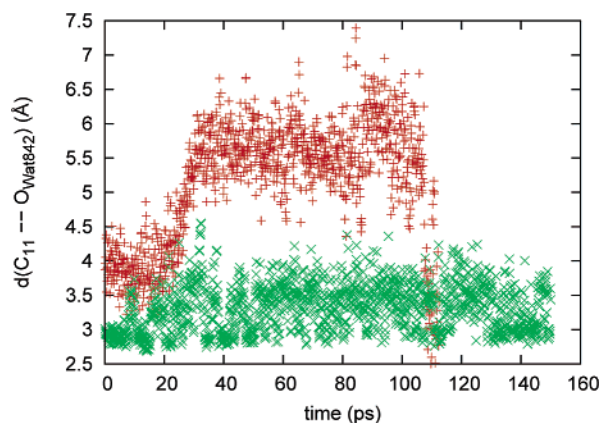

Figure 8. Evolution of the distance between the donor and the acceptor atoms at the Michaelis complex: wild-type (in green) and Ile553Ala mutant (in red). The first 30 ps correspond to the heating period of the MD simulation.

over bins with 0.01 Å width. Importantly, the geometric proximity in terms of z between the reactants and the transition state is only 0.5 Å, in such a way that the donor−acceptor average distance decreases in 0.3 Å (Figure 7). In contrast, from the transition state to the products, the donor−acceptor average distance increases by almost 1 Å. Thus, the change of the donor−acceptor distance along the hydrogen transfer reaction is more asymmetric than the ones obtained in other enzymatic studies for the same type of reaction.[65,66] Probably, this fact is a consequence of the specific geometric characteristics of the SLO-1 active site, which highly compress the donor−acceptor distance at the reactant Michaelis complex. As a consequence, the reaction path turns out to be very narrow.

At this point, it is worth mentioning that the substitution of the residue Ile553 by an Ala residue clearly changes this special characteristic of the wild-type enzyme. As shown in Figure 8, during the MD simulation of the mutant enzyme at the reactant configuration, the donor−acceptor distance increases and fluctuates more with respect to the wild-type form. As a matter of fact, in the particular snapshots shown in Figure 3 it can be seen that the distance between the H_{11A} donor and acceptor atoms is 3.44 Å for the wild-type enzyme but 5.52 Å for the mutant enzyme. This suggests that the reaction coordinate distance between R and TS or P will be larger in the mutant. These theoretical results further support the proposal by Klinman and co-workers of a more relaxed active site in the Ile553Ala mutant.[64]

The computed classical free energy of activation, ΔG_{act}^{CM}, is 11.0 and 10.9 kcal/mol, for the protium and deuterium transfers,
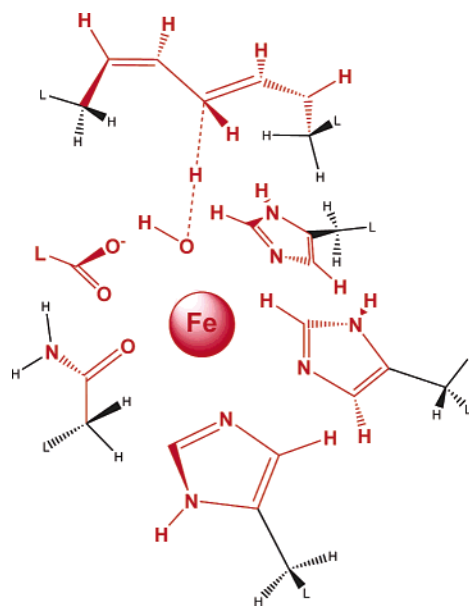

Figure 9. Schematic representation of the 48 primary zone atoms (in red) defined in the text. The link atoms are labeled with an L.

respectively, which includes the correction due to the free energy of the normal mode that corresponds to z at z_R. It turns out that this correction, which is calculated by a procedure that has been presented previously,[31] is 0.4 kcal/mol for the system with a protium at the H_{11A} position and 0.5 kcal/mol for the system with a deuterium at this position. Note that the difference between ΔG_{act}^{CM} and $\Delta G_{act}^{(1)}$ comes from the absence in the former of the quantized-vibrational correction for the nuclei in the predefined primary zone.

3.2.1. Structural Analysis of the Interactions in the Active Site. The last three columns of Table 1 show the evolution of selected distances along the calculated reaction path. We have defined three groups of configurations that were generated and saved in the umbrella sampling trajectory, corresponding to the Michaelis complex: the reactant region (defined by the range of $z = z_R \pm 0.250$ Å), the transition state (defined by $z = -0.095 \pm 0.100$ Å), and the product region (defined by $z = z_P \pm 0.250$ Å). The values reported in Table 1 for the reactant, TS, and product correspond to averaged distances over these three groups of configurations. In general, the Fe−ligand distances do not significantly change during the reaction. The Fe−Asn694 distance is constant, and the Fe−Wat842 distance is aproximatively constant, in contrast to the reaction profile calculated for a gas-phase model of the active site.[24]

The LA substrate has very few interactions with the enzymatic residues due to its hydrophobicity. In particular, we have only found two important interactions: the LA-Trp500 $\pi-\pi$ stacking interaction, which as mentioned above, has also been confirmed by X-ray crystallography,[34] and which is maintained along the calculated reaction path (see Table 1), and the LA-Gln495 hydrogen bond interaction, which is formed in going from the reactant to the product.

3.3. Degree of Tunneling and Rate Constants. In the EA-VTST/MT method the rate constant is formulated as the product of two factors.[31,32] The second factor (see eq 4), called the quasithermodynamic factor, is calculated from the classical mechanical free energy barrier obtained in the previous section after adding the effect of quantizing all the degrees of freedom perpendicular to the reaction coordinate for the primary zone atoms defined in Figure 9, which leads to the generalized free energy of activation in eq 2. The first factor, the transmission

TABLE 2: Free Energies of Activation (kcal/mol) and Average Transmission Coefficients at 303 K for Protium and Deuterium with Standard Deviations in Parentheses

isotope	ΔG_{act}^{CM}	$\Delta G_{act}^{(1)}$	$\langle \Gamma_i \rangle$	$\langle \kappa_i \rangle$	$\langle \gamma_i \rangle$	$\Delta G_{act}^{EA-VTST/MT}$
H	10.97	7.15	0.966 $_{(0.031)}$	432$_{(393)}$	407$_{(353)}$	3.53
D	10.93	8.09	0.966 $_{(0.032)}$	215$_{(143)}$	204$_{(128)}$	4.89
H^a				3.12×10^7		
D^a				1.65×10^6		

	kinetic isotope effects		
	KIE$_{vib}$	KIE$_{tunnel}$	KIE$_{total}$
	4.76	2.00	9.52
final estimation^a	4.76	18.85	89.75

^{a} Results obtained for one configuration after raising the adiabatic potential energy barrier by 10 kcal/mol, which will match the experimental and calculated protium abstraction rate constants (see Section 3.4).

TABLE 3: Dynamical Effects for Each Configuration with Protium or Deuterium at Position 11A^a

conf	isotope	$V^{\ddagger}$	V^{AG}	κ_i	Γ_i	γ_i	KIE$_{tunnel}$	KIE$_{total}$
1	H	13.94	8.20	1176	0.910	1070		
	D	13.94	9.36	478	0.912	436	2.45	11.66
2	H	12.45	7.38	462	0.970	448		
	D	12.45	8.52	238	0.971	231	1.94	9.23
3	H	12.26	6.82	246	0.996	245		
	D	12.26	7.98	160	0.999	160	1.53	7.28
4	H	11.51	6.03	217	0.995	216		
	D	11.51	7.18	142	0.997	142	1.52	7.24
5	H	9.65	4.33	61	0.957	58		
	D	9.65	5.47	56	0.951	53	1.10	5.24

^{a} Potential energy barrier $V^{\ddagger}$, adiabatic potential energy barrier V^{AG}, individual transmission coefficients, tunneling contribution to the KIE, and total KIE. Energies are given in kcal/mol.

coefficient $\gamma(T)$, accounts for the quantum effects on the reaction coordinate, that is, tunneling and nonclassical reflection, and for dynamical recrossing.

We have calculated the quantum correction to the vibrational free energy, ΔW_{vib}, obtained for the protium and deuterium substitution, respectively, and the effect of adding this correction to the CM PMF is shown in Figure 6. As expected, the effect of quantizing vibrations is larger in the lighter isotope, giving rise to what is called the vibrational KIE, as will be presented in the next section. Thus, the generalized free energy of activation, $\Delta G_{act}^{(1)}$ in Table 2, is 7.2 and 8.1 kcal/mol for the protium and deuterium substitutions, respectively. There is no displacement in the location of the transition state from the classical PMF due to the inclusion of quantizing vibrations.

For the calculation of the first factor, we used five configurations to represent the transition state ensemble (TSE), which were chosen with the criterium explained in Section 2.3.3. Note that in previous papers where the EA-VTST/MT method has been applied to calculate dynamical and quantum effects different numbers of configurations between 5 and 20 have been used.[32,67] For each of the five configurations selected here, a saddle point structure was localized under the SSZ approximation. Then, the minimum energy path (MEP) for each isotope substitution was obtained. Table 3 shows the values of the potential energy and the adiabatic potential energy barriers of these individual paths. The individual MEPs were used to determine the individual transmission factors, Γ_i and κ_i in Table 3. Table 2 indicates that the average value of the quasiclassical recrossing factor for the protium substitution is 0.97 and its standard deviation is 0.03, which denotes that this factor has very small fluctuations among the different configurations. On

the contrary, the individual values of the semiclassical transmission coefficient can be divided into three groups of small ($\leq$100), medium ($\leq$1000), or large ($\geq$1000) κ_i values, depending on the compression of the active site, which has been quantitatively characterized by the dihedral angles formed between the lipid tails and the hydrogen donor−acceptor bond (see Section 2.3.3). Three configurations belong to the second group, but we have only a represent configuration for the other two. As a result, the average value of κ_i and its standard deviation are 432 and 393, respectively. Note that the standard deviation is a measure of the heterogeneity of the transition state members and reflects the dispersion in the histogram of the κ_i values.

The seventh column of Table 3 lists the net transmission coefficients for the five configurations, γ_i, which averaged over them gives a value of 407 for the final ensemble-averaged transmission coefficient, γ, with a standard deviation of 353 (see Table 2). As mentioned above and also found in previous studies,[46,49] the high value of the standard deviation is due to the fluctuations of the individual barrier heights (see the third and fourth columns of Table 3) and widths (see Figure 10) of the adiabatic potentials used to calculate the tunneling correction for each of the configurations in a canonical ensemble of transition states.

Including quantum mechanical tunneling and quasiclassical dynamical recrossing corrections, we have obtained the final values of the EA-VTST/MT rate constant (eq 4) for the protium and the deuterium substitutions, from which we estimate the phenomenological free energy of activation values (eq 5) of 3.5 and 4.9 kcal/mol, respectively. Table 2 summarizes the values of the energies of activation obtained for the protium and the deuterium reactions at the different stages of our calculation. The phenomenological free energy of activation theoretically obtained for the protium transfer is 10.7 kcal/mol smaller than the value obtained from the experimental rate constant ($k_{cat} = 297$ s^{-1}).[64] The difference between the experimental and the theoretical value is probably the consequence of the recently reported underestimation of reaction barriers of proton-coupled electron-transfer processes by the B3LYP method.[68] The further improvement of the QM level will quantitatively approach the theoretical and the experimental results.

The results obtained up to now, which explicitly include both the quantum effects and the protein conformational flexibility, can give an indication of the degree of tunneling for the two reactive processes studied (protium and deuterium transfers) in this enzyme. That is, from the $k^{QC}(T)$ and $k(T)^{EA-VTST/MT}$ rate constants (eqs 3 and 4, respectively), we estimate a lower limit of the degree of tunneling (the fraction of reactions that occur by tunneling)[49] as follows:

$$F_{tun} \geq \frac{k^{EA-VTST/MT} - k^{QC}}{k^{EA-VTST/MT}} \qquad (6)$$

This quantum effect accounts for more than 99% of the rate constants of the protium and the deuterium transfers. However, this result is biased by the understimation of the potential energy barrier obtained with the QM/MM potential used in this work (which has been commented on in the previous paragraph). However, a more accurate QM/MM potential energy surface, which is expected to increase the adiabatic potential energy barrier, will even increase the degree of tunneling for both isotopes. This is further analyzed in the next section.

3.4. Primary Kinetic Isotope Effect. The ratio between the $k^{(1)}$ values obtained for the protium and deuterium transfers gives
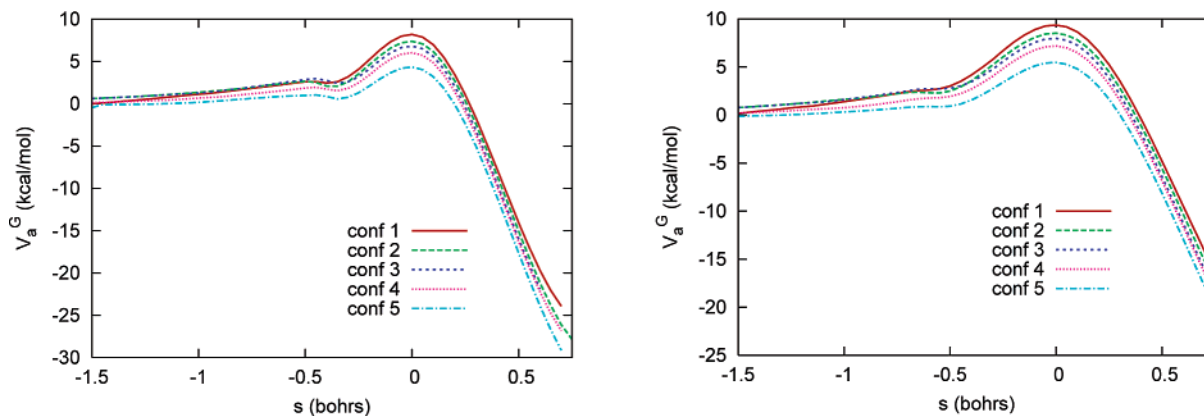
Figure 10. Adiabatic potential energy profiles: protium on the left side and deuterium on the right side. s is the arc length along the corresponding MEPs in mass-scaled coordinates. $s = 0$ at the saddle point, whereas negative and positive values correspond to the reactant and product regions, respectively.

a vibrational KIE of 4.8, which is a quite high value in comparison with the ones obtained for other hydrogen transfer reactions studied with the same theoretical method,[31,46,48,49] but similar to the one obtained for methylamine dehydrogenase,[69] another enzyme with an unusually large primary KIE. This result further validates our statment of the importance of including quantum effects, such as the zero point energy, in the calculation of KIEs.[70]

The quasiclassical KIE is calculated as the ratio between de protium and the deuterium values of the k^{QC} rate constant. In this particular study, it results in identical vibrational KIE because the classical recrossing does not contribute to the KIE.

$$KIE_{tunnel} = \frac{(\gamma/\Gamma)_H}{(\gamma/\Gamma)_D} \qquad (7)$$

On the other hand, eq 7 gives the tunneling contribution to the KIE, that is 2.0, as shown in Table 2.

Up to this point we have carried out electronic structure/ dynamical calculations without any fitting to the experimental results available for this reaction. In this way we have obtained a detailed microscopical picture of how the enzyme works, showing the great relevance of tunneling. However, from the quantitative point of view, the calculated phenomenological free energy of activation turns out to be 10.7 kcal/mol smaller than the experimental one for the protium abstraction, and the final calculated primary KIE is 9.5, which is larger than the classical limit, but quite a bit smaller than the values of the experimentally determined KIE, probably due to an underestimation of the tunneling contribution. Then it seems that to match the experimental and calculated protium abstraction rate constants a vertical shift of about 10 kcal/mol of the potential energy barrier would be required. This procedure is acceptable as we are not trying to reproduce the numerical value of the rate constant, but the KIE, and can be regarded as analogous to fittings used in previous studies of this system to reproduce the experimental rate constant or the experimental KIE.[28,29] The point now is whether doing this shifting our SLO-1 model would be capable of reproducing the experimental KIE. To check this we have calculated how the tunneling associated with the configuration of the transition state ensemble with a highest value of κ_i in Table 3 (configuration 1) is altered when its reaction path is modified in such a way that the potential energy barrier is raised almost 10 kcal/mol (from 13.94 kcal/mol to 23.5 kcal/mol). The modified potential energies are obtained by adding a correction function $\Delta V(s)$ to the original potential energies of this test configuration. The analytic function for

$\Delta V(s)$ is obtained by using the interpolation method based on corrections at different points on the reaction path.[71−73] $\Delta V(s)$ is formed by two different functions at each side of the saddle point: one was built considering the saddle point and the reactant well plus one additional point between them, whereas the other was built following the same procedure but for the product side. For the correction function $\Delta V(s)$, we used a cutoff Gaussian of the form

$$\Delta V = A_R \exp\left(-\frac{B_R}{1 - \left(\frac{s}{s_{RW}}\right)^2}\right) + C_R \qquad (8)$$

where

$$A_R = [\Delta V^{\ddagger} - \Delta V(s = s_{RW})]\exp(B_R) \qquad (9a)$$

$$C_R = \Delta V(s = s_{RW}) \qquad (9b)$$

The value of ΔV at $s = 0$ is denoted $\Delta V^{\ddagger}$; B_R and B_P are the range parameters for reactants and products, respectively; s_{RW} and s_{PW} indicate the location of the reactant and the product well, respectively. Each cutoff Gaussian correction function branch is solely determined by the correction at $s = 0$ and either at $s = s_{RW}$ or s_{PW}. B_R (or B_P) is determined by first fitting a cutoff Gaussian function to the original reaction path at $s = 0$, $s = s_{RW}$ (or s_{PW}), and at an additional intermediate point. All the Gaussian-modified PESs were computed by using the POLYRATE9.3 code.[53] The values of the parameters turn out to be $B_R = 52.68$, $B_P = 35.25$, $s_{RC} = -3.22$ bohr, and $s_{PC} = 5.81$ bohr for the protium abstraction, and $B_R = 31.07$, $B_P = 20.93$, $s_{RC} = -3.35$ bohr, and $s_{PC} = 6.2$ bohr for the deuterium abstraction. The row corresponding to curve 2 in Table 4 exhibits the semiclassical transmission coefficients for protium and deuterium abstractions obtained through the new adiabatic potential energy curve (now based on a potential energy barrier of 23.5 kcal/mol) associated with configuration 1, along with the corresponding tunneling contribution to the KIE and the total KIE (remember that the vibrational contribution is 4.8). As can be seen, huge values of κ_1 are now obtained, in such a way that the tunneling contribution to the KIE changes from a value of 2.45 for the original reaction path to 18.85 for the one with the increased potential energy barrier, while the total KIE is as great as 89.75, in very good accordance with the experimental results. In other words, with the right value of the potential energy barrier, the KIE arising from our micro- scopical model and the experimental one practically match.

TABLE 4: Results Corresponding to the New Adiabatic Potential Energy Curves Associated with Configuration 1 (see text): s_{RC} and s_{PC} Parameters (bohr), Semiclassical Transmission Coefficients for Protium and Deuterium, Tunneling Contribution to the KIE, and Total KIE. Power of 10 in Parentheses

curve	s_{RC}	s_{PC}	$\kappa_{1,H}$	$\kappa_{1,D}$	KIE$_{tunnel}$	KIE$_{total}$
1	−2.0	3.0	1.20(+08)	1.21(+07)	9.91	47.16
2	−3.22	5.81	3.12(+07)	1.65(+06)	18.85	89.75
3	−4.0	7.0	1.65(+07)	6.85(+05)	24.12	114.82
4	−6.0	8.0	3.14(+06)	9.70(+04)	32.41	154.30
5	−7.0	10.0	1.30(+06)	3.91(+04)	33.36	158.81
6	−9.0	15.0	2.70(+05)	9.98(+03)	27.10	129.02
7	−10.0	20.0	1.36(+05)	6.08(+03)	22.47	106.96
8	−12.0	30.0	4.54(+04)	3.03(+03)	14.96	71.23

Another point that merits being analyzed is the sensitivity of the KIE to the reaction path width. To check this, we have built up a set of new reaction paths corresponding to configuration 1, varying the width of the reaction path, but keeping unchanged the value of 23.5 kcal/mol for the potential energy barrier. To do this, the B_R and B_P parameters of the cutoff Gaussian correction function have been kept unchanged, whereas the parameters s_{RC} and s_{PC} have been modulated and taken as equivalents for both H and D isotopes. The results obtained for the new set of adiabatic potential energy curves after inclusion of the vibrational corrections (see Figure 11) are also shown in Table 4.

The width of the curves increases from curves 1 to 8. As expected, it can be seen that the larger the width, the smaller the semiclassical transmission coefficients for both the protium and deuterium abstractions. Thus, decompressing the active center will result in a lower contribution of tunneling to the reaction rate, thus indicating the importance of the proposed[64] gating promoting mode. On the other hand, the tunneling contribution to the KIE (and, as a consequence, the total KIE) also exhibits an important dependence on the barrier width. The greater KIE values correspond to the intermediate barrier width values, because as the barrier becomes narrower tunneling increases, but the ratio between the H and D quantal transmission probabilities through the barrier diminishes. These results confirm that the KIE highly depends on the distance that the hydrogen atom has to jump along the abstraction process. In view of the results (see Figure 11 and Table 4), it seems that our uncorrected model (without the vertical shift of the potential energy barrier) is able to reproduce the barrier width but not the barrier height that leads to the experimental KIE.
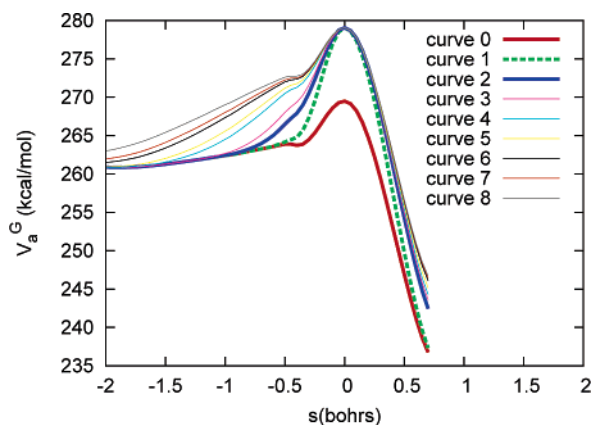

Figure 11. Set of adiabatic potential energy curves built up to analyze the dependence of the KIE on the height and the width of the barrier (see text). Curve 0 stands for the configuration 1 original curve. Curve 2 corresponds to the profile obtained by only modifying the barrier height.

4. Conclusions

In this paper we present a fully microscopical simulation of the rate-limiting hydrogen abstraction from linoleic acid by the Fe(III)-OH$^-$ cofactor in soybean lipoxygenase-1. We have studied the complete enzyme with the corresponding solvation shell of water molecules, including the real substrate (linoleic acid). We have used a QM/MM hybrid method to describe the potential energy surface of the whole system, and the ensemble-averaged variational transition-state theory with multidimensional tunneling (EA-VTST/MT) to calculate the rate constant and the corresponding H/D primary kinetic isotope effect. The quantum mechanical subsystem in the QM/MM electronic structure calculations has been described by our own semiempirical PM3/d model with specific reaction parameters for iron fitted to reproduce B3LYP/6-311++G(3df,2p)/MM results.

We have shown that the hydrogen donor−hydrogen acceptor distance at the reactant Michaelis complex is highly compressed and rigid in the wild-type enzyme, but it becomes larger and more flexible in the Ile553Ala mutant. This result is a consequence of the substitution of a bulky residue that compresses the linoleic acid against the iron cofactor by an alanine, which allows some expansion of the substrate-binding pocket, in accordance with the experimental results based on site-directed mutagenesis.[64] As a consequence of the compression, in the wild-type SLO-1 the adiabatic energy barrier is very narrow, in such a way that tunneling turns out to be huge, accounting for more than 99% of the rate constants corresponding to the protium and deuterium abstractions at 303 K. In contrast, in the mutant, the more relaxed active site gives rise to the proposed[64] key role of the gating promoting mode in the hydrogen abstraction in SLO-1. The huge contribution of tunneling in this reaction has been inferred from those previous experimental results and theoretical models, and is here confirmed by a completed microscopical model of the substrate−enzyme complex. After applying a correction to the potential energy barrier of the hydrogen abstraction, we have reproduced the enormous experimental KIE. Anyway, despite the huge tunneling acting in the reaction, an important part of the total KIE comes from the vibrational contribution, which affords a factor of 4.8. In addition, it has been shown that the KIE has an important dependence on the barrier width.

The results presented in this work open the possibility to extend this kind of complete microscopical treatment to the study of the temperature dependence of the rate constants and H/D kinetic isotope effects in the wild-type SLO-1 and different mutants of it. Work covering these aspects is now in progress in our group.

References and Notes

(1) Prigge, S. T.; Boyington, J. C.; Faig, M.; Doctor, K. S.; Gaffney, B. J.; Amzel, L. M. *Biochimie* **1997**, *79*, 629−636.

(2) Prigge, S. T.; Boyington, J. C.; Gaffney, B. J.; Amzel, L. M. *Proteins* **1996**, *24*, 275−291.

(3) Yu, M. K.; Moos, P. J.; Cassidy, P.; Wade, M.; Fitzpatrick, F. A. *J. Biol. Chem.* **2004**, *279*, 28028−28035.

(4) Rioux, N.; Castonguay, A. *Carcinogenesis* **1998**, *19*, 1393−1400.

(5) Moody, T. W.; Leyton, J.; Martinez, A.; Hong, S.; Malkinson, A.; Mulshine, J. L. *Exp. Lung. Res.* **1998**, *24*, 617−628.

(6) Knapp, M. J.; Klinman, J. P. *Eur. J. Biochem.* **2002**, *269*, 3113−3121.

(7) Solomon, E. I.; Brunold, T. C.; Davis, M. I.; Kemsley, J. N.; Lee, S. K.; Lehnert, N.; Neese, F.; Skulan, A. J.; Yang, Y. S.; Zhou, J. *Chem. Rev.* **2000**, *100*, 235−349.

(8) Rickert, K. W.; Klinman, J. P. *Biochemistry* **1999**, *38*, 12218−12228.

(9) Moiseyev, N.; Rucker, J.; Glickman, M. H. *J. Am. Chem. Soc.* **1997**, *119*, 3853−3860.

(10) Kohen, A.; Klinman, J. P. *Acc. Chem. Res.* **1998**, *31*, 397−404.

(11) Minor, W.; Steczko, J.; Stec, B.; Otwinowski, Z.; Bolin, J. T.; Walter, R.; Axelrod, B. *Biochemistry* **1996**, *35*, 10687−10701.

(12) Meyer, M. P.; Klinman, J. P. *Chem. Phys.* **2005**, *319*, 283−296.

(13) Liang, Z. X.; Klinman, J. P. *Curr. Opin. Struct. Biol.* **2004**, *14*, 648−655.

(14) Kohen, A. *Prog. React. Kinet. Mech.* **2003**, *28*, 119−156.

(15) Knapp, M. J.; Rickert, K.; Klinman, J. P. *J. Am. Chem. Soc.* **2002**, *124*, 3865−3874.

(16) Glickman, M. H.; Wiseman, J. S.; Klinman, J. P. *J. Am. Chem. Soc.* **1994**, *116*, 793−794.

(17) Kohen, A. *Prog. React. Kinet. Mech.* **2003**, *28*, 119−156.

(18) Masgrau, L.; Roujeinikova, A.; Johannissen, L. O.; Hothi, P.; Basran, J.; Ranaghan, K. E.; Mulholland, A. J.; Sutcliffe, M. J.; Scrutton, N. S.; Leys, D. *Science* **2006**, *312*, 237−241.

(19) Hammes-Schiffer, S. *Acc. Chem. Res.* **2006**, *39*, 93−100.

(20) Garcia-Viloca, M.; Gao, J.; Karplus, M.; Truhlar, D. G. *Science* **2004**, *303*, 186−195.

(21) Borowski, T.; Krol, M.; Chruszcz, M.; Broclawik, E. *J. Phys. Chem. B* **2001**, *105*, 12212−12220.

(22) Lehnert, N.; Solomon, E. I. *J. Biol. Inorg. Chem.* **2003**, *8*, 294−305.

(23) Borowski, T.; Broclawik, E. *J. Phys. Chem. B* **2003**, *107*, 4639−4646.

(24) Tejero, I.; Eriksson, L. A.; González-Lafont, A.; Marquet, J.; Lluch, J. M. *J. Phys. Chem. B* **2004**, *108*, 13831−13838.

(25) Kuznetsov, A. M.; Ulstrup, J. *Can. J. Chem.* **1999**, *77*, 1085−1096.

(26) Tresadern, G.; McNamara, J. P.; Mohr, M.; Wang, H.; Burton, N. A.; Hillier, I. H. *Chem. Phys. Lett.* **2002**, *358*, 489−494.

(27) Siebrand, W.; Smedarchina, Z. *J. Phys. Chem. B* **2004**, *108*, 4185−4195.

(28) Olsson, M. H. M.; Siegbahn, P. E. M.; Warshel, A. *J. Am. Chem. Soc.* **2004**, *126*, 2820−2828.

(29) Hatcher, E.; Soudackov, A. V.; Hammes-Schiffer, S. *J. Am. Chem. Soc.* **2004**, *126*, 5763−5775.

(30) Warshel, A.; Levitt, M. *J. Mol. Biol.* **1976**, *103*, 227−249.

(31) Alhambra, C.; Corchado, J.; Sánchez, M. L.; Garcia-Viloca, M.; Gao, J.; Truhlar, D. G. *J. Phys. Chem. B* **2001**, *105*, 11326−11340.

(32) Truhlar, D. G.; Gao, J.; Garcia-Viloca, M.; Alhambra, C.; Corchado, J.; Sánchez, M. L.; Poulsen, T. D. *Int. J. Quantum Chem.* **2004**, *100*, 1136−1152.

(33) Minor, W.; Steczko, J.; Stec, B.; Otwinowski, Z.; Bolin, J. T.; Walter, R.; Axelrod, B. *Biochemistry* **1996**, *35*, 10687−10701.

(34) Skrzypczak-Jankun, E.; Bross, R. A.; Carroll, R. T.; Dunham, W. R.; Funk, M. O. *J. Am. Chem. Soc.* **2001**, *123*, 10814−10820.

(35) http://www.bioinf.org.uk/software/profit.

(36) Brooks, B. R.; Bruccoleri, R. E.; Olafson, B. D.; States, D. J.; Swaminathan, S.; Karplus, M. *J. Comput. Chem.* **1983**, *4*, 187−217.

(37) Thiel, W. *MNDO97*; Organisch-chemisches Institut, Universität Zürich: Zürich, Switzerland 1998.

(38) Reuter, N.; Dejaegere, A.; Maigret, B.; Karplus, M. *J. Phys. Chem. A* **2000**, *104*, 1720−1735.

(39) MacKerell, A. D.; Bashford, D.; Bellott, M.; Dunbrack, R. L.; Evanseck, J. D.; Field, M. J.; Fischer, S.; Gao, J.; Guo, H.; Ha, S.; Joseph-McCarthy, D.; Kuchnir, L.; Kuczera, K.; Lau, F. T. K.; Mattos, C.; Michnick, S.; Ngo, T.; Nguyen, D. T.; Prodhom, B.; Reiher, W. E.; Roux, B.; Schlenkrich, M.; Smith, J. C.; Stote, R.; Straub, J.; Watanabe, M.; Wiorkiewicz-Kuczera, J.; Yin, D.; Karplus, M. *J. Phys. Chem. B* **1998**, *102*, 3586−3616.

(40) Jorgensen, W. L.; Chandrasekhar, J.; Madura, J. D.; Impey, R. W.; Klein, M. L. *J. Chem. Phys.* **1983**, *79*, 926−935.

(41) Feller, S. E.; MacKerell, A. D. *J. Phys. Chem. B* **2000**, *104*, 7510−7515.

(42) González-Lafont, A.; Truong, T. N.; Truhlar, D. G. *J. Phys. Chem.* **1991**, *95*, 4618−4627.

(43) Tejero, I.; González-Lafont, A.; Lluch, J. M. *J. Comput. Chem.*, in press.

(44) Brooks, C. L.; Karplus, M. *J. Mol. Biol.* **1989**, *208*, 159−181.

(45) Brooks, C. L.; Karplus, M. *J. Chem. Phys.* **1983**, *79*, 6312−6325.

(46) Poulsen, T. D.; Garcia-Viloca, M.; Gao, J.; Truhlar, D. G. *J. Phys. Chem. B* **2003**, *107*, 9567−9578.

(47) Ryckaert, J. P.; Ciccotti, G.; Berendsen, H. J. C. *J. Comput. Phys.* **1977**, *23*, 327−341.

(48) Garcia-Viloca, M.; Alhambra, C.; Truhlar, D. G.; Gao, J. *J. Comput. Chem.* **2003**, *24*, 177−190.

(49) Garcia-Viloca, M.; Truhlar, D. G.; Gao, J. *Biochemistry* **2003**, *42*, 13558−13575.

(50) Kumar, S.; Bouzida, D.; Swendsen, R. H.; Kollman, P. A.; Rosenberg, J. M. *J. Comput. Chem.* **1992**, *13*, 1011−1021.

(51) Roux, B. *Comput. Phys. Commun.* **1995**, *91*, 275−282.

(52) Garcia-Viloca, M.; Alhambra, C.; J. Corchado, M. L. S.; Villa, J.; Gao, J.; Truhlar, D. G. *CHARMMRATE*, version 2.0; University of Minnesota: Minneapolis, MN, 2002.

(53) Corchado, J. C.; Chuang, Y.-Y.; Fast, P. L.; Villà, J.; Hu, W.-P.; Liu, Y.-P.; Lynch, G. C.; Nguyen, K. A.; Jackels, C. F.; Melissas, V. S.; Lynch, B. L.; Rossi, I.; Coitiño, E. L. C.; Fernández-Ramos, A.; Pu, J.; Albu, T. V.; Steckler, R.; Garret, B. C.; Isaacson, A. D.; Truhlar, D. G. *POLYRATE 9.3*; University of Minnesota: Minneapolis, MN, 2004; http://comp.chem.umn.edu/polyrate.

(54) Garcia-Viloca, M.; Alhambra, C.; Truhlar, D. G.; Gao, J. *J. Chem. Phys.* **2001**, *114*, 9953−9958.

(55) Alhambra, C.; Corchado, J.; Sánchez, M. L.; Garcia-Viloca, M.; Gao, J.; Truhlar, D. G. *J. Phys. Chem. B* **2001**, *105*, 11326−11340.

(56) Truhlar, D. G.; Isaacson, A. D.; Garrett, B. C. *Theory of Chemical Reaction Dynamics*; CRC Press: Boca Raton, FL, 1985; p 65.

(57) Press, W. H.; Flannery, B. P.; Teukolsky, S. A.; Vetterling, W. T. *Numerical Recipes*: *The Art of Scientific Computing*, 2nd ed.; Cambridge University Press: Cambridge (UK) and New York, 1992.

(58) Garrett, B. C.; Redmon, M. J.; Steckler, R.; Truhlar, D. G.; Baldridge, K. K.; Bartol, D.; Schmidt, M. W.; Gordon, M. S. *J. Phys. Chem.* **1988**, *92*, 1476−1488.

(59) Liu, Y. P.; Lynch, G. C.; Truong, T. N.; Lu, D. H.; Truhlar, D. G.; Garrett, B. C. *J. Am. Chem. Soc.* **1993**, *115*, 2408−2415.

(60) Zhang, Y.; Gan, Q. F.; Pavel, E. G.; Sigal, E.; Solomon, E. I. *J. Am. Chem. Soc.* **1995**, *117*, 7422−7427.

(61) Ruddat, V. C.; Mogul, R.; Chorny, I.; Chen, C.; Perrin, N.; Whitman, S.; Kenyon, V.; Jacobson, M. P.; Bernasconi, C. F.; Holman, T. R. *Biochemistry* **2004**, *43*, 13063−13071.

(62) Schenk, G.; Neidig, M. L.; Zhou, J.; Holman, T. R.; Solomon, E. I. *Biochemistry* **2003**, *42*, 7294−7302.

(63) Lehnert, N.; Solomon, E. I. *J. Biol. Inorg. Chem.* **2003**, *8*, 294−305.

(64) Knapp, M. J.; Rickert, K.; Klinman, J. P. *J. Am. Chem. Soc.* **2002**, *124*, 3865−3874.

(65) Agarwal, P. K.; Billeter, S. R.; Rajagopalan, P. T. R.; Benkovic, S. J.; Hammes-Schiffer, S. *Proc. Natl. Acad. Sci. U.S.A.* **2002**, *99*, 2794−2799.

(66) Agarwal, P. K.; Billeter, S. R.; Hammes-Schiffer, S. *J. Phys. Chem. B* **2002**, *106*, 3283−3293.

(67) Pu, J. Z.; Gao, J.; Truhlar, D. G. *Chem. Rev.* **2006**, *106*, 3140−3169.

(68) Lingwood, M.; Hammond, J. R.; Hrovat, D. A.; Mayer, J. M.; Borden, W. T. *J. Chem. Theory Comput.* **2006**, *2*, 740−745.

(69) Alhambra, C.; Sánchez, M. L.; Corchado, J. C.; Gao, J.; Truhlar, D. G. *Chem. Phys. Lett.* **2002**, *355*, 388−394.

(70) Truhlar, D. G.; Gao, J.; Alhambra, C.; Garcia-Viloca, M.; Corchado, J.; Sánchez, M. L.; Villà, J. *Acc. Chem. Res.* **2002**, *35*, 341−349.

(71) Hu, W. P.; Liu, Y. P.; Truhlar, D. G. *J. Chem. Soc., Faraday Trans.* **1994**, *90*, 1715−1725.

(72) Chuang, Y. Y.; Truhlar, D. G. *J. Phys. Chem. A* **1997**, *101*, 8741−8741.

(73) Chuang, Y. Y.; Truhlar, D. G. *J. Phys. Chem. A* **1997**, *101*, 3808−3814.